Adv Syst Sci Appl 2022; **03**:49–69
Published online at https://ijassa.ipu.ru.

Model of Calcium Dynamics Regulating IP_3 and ATP Production in a Fibroblast Cell

Ankit Kothiya*, Neeru Adlakha

Department of Mathematics and Humanities, SVNIT, Surat-395 007, Gujarat, India

Abstract: Fibroblast cells are involved in the mechanism of growth and repair of tissue in human organs. Calcium (Ca^{2+}) signaling is essentially required to maintain the microstructure and physiological function of the fibroblast cell. The study of Ca^{2+} signaling in fibroblast cells is crucial to understanding the mechanisms and disorders of fibroblast cells. The inositol 1,4,5-trisphosphate (IP_3) participates in the release and extension of calcium from the endoplasmic reticulum (ER). Adenosine triphosphate (ATP) also regulate various biological activity like proliferation, migration, stimulation of cell growth, etc. Any disturbance in Ca^{2+} can disturb the levels of IP_3 and ATP in the cell. The Ca^{2+} dynamics and its relationship with IP_3 and ATP production are not well understood. There is a need to understand the relationship among various parameters of Ca^{2+} dynamics and its role in IP_3 and ATP production. The Ca^{2+} dynamics in fibroblast have been investigated by several researchers, but no attention is reported for analyzing Ca^{2+} dynamic production of IP_3 and ATP. A mathematical model is proposed for analyzing the role of Ca^{2+} signaling in the production of IP_3 and ATP in fibroblast cells. The model incorporates the effect of diffusion, buffer, leak, sarco endoplasmic reticulum calcium ATPase ($SERCA$) pump, etc. The model is formulated in the form of an initial-boundary problem. The solution is obtained using the finite element approach. The effects of excessive or low values of various parameters on Ca^{2+} dynamics, ATP production, IP_3 production, and IP_3 degradation have been analyzed for possible disorders in functions of a fibroblast cell. The alterations in these parameters cause alterations in ATP production, IP_3 production and IP_3 degradation and Ca^{2+} concentration profiles. This alteration in parameters can be responsible for the function and dysfunction of fibroblast cells, leading to cardiac disease, fibrosis, delayed wound healing, etc. The results lead to conclusion that the changes in source influx, buffers, and diffusion coefficient can cause an increase or decrease in ATP and IP_3 production and IP_3 degradation leading to disorders of fibroblast cells like cardiac fibroblast cell proliferation and migration, which have a role in wound healing, inflammation, and cancer . Obtained results provide insights into the Ca^{2+}-dependent production of IP_3 and ATP in a fibroblast cell. These insights can be useful for developing diagnostics and treating disorders of fibroblast cells.

Keywords: IP_3 receptor, $SERCA$ pump, ATP, finite element method, calcium, fibroblast cell

1. INTRODUCTION

Every system of an organism is made up of various types of cells. The functions of an organism are achieved by the cellular mechanism in the cell. One of the primary functions is to communicate with each part of the body and accomplish by Intra and inter-cellular calcium signaling [3]. A fibroblast is a kind of organic cell that originates locally from mesenchymal cells and is a permanent resident of connective tissue. These mesenchymal cells produce extracellular matrices such as collagens, fibronectin, tenascin and proteoglycans. It creates the auxiliary system for creature tissues and assumes a basic job in the healing of

*Corresponding author: ankitkothiya1996@gmail.com

wounds [32]. Fibroblast cells are virtually present in every tissue of our body. They are responsible for the three-dimensional architecture and mechanical strength of the tissue. It maintains the structural framework in the tissue of animals by the synthesis of extracellular matrix molecules [33]. The change in fibroblast number and properties are associated with chronic lung diseases. The alteration in injury repair is responsible for asthma and pulmonary fibrosis [23]. Fibroblast cell plays a vital role in chronic lung disease. Transforming growth factor-beta (TGF-β) regulates the fibroblast function. Fibroblast response to cytokines, pro-inflammatory mediators and a variety of growth factors. The role of Ca^{2+} signaling in these responses is still not well explored [22].

Intracellular free Ca^{2+} is a ubiquitous secondary messenger, and it regulates various physiological processes like metabolism, differentiation, proliferation, signal transduction, secretion and contraction [15]. There are various types of buffers found in the fibroblast cell. Also, referred as proteins, buffer binds with Ca^{2+} to reduce the intracellular Ca^{2+} in fibroblast cells. There are many types of signaling processes in fibroblast cells that elevate intracellular Ca^{2+} and initiate activities of the cell. Two major mechanisms release Ca^{2+} from intracellular stores. These are the ryanodine receptor (RyR) and IP_3 receptors activations in a cell. The RyR receptor is reported to be absent in humans and rate cardiac fibroblast [5]. However, TGF-β acts on ryanodine sensitive channel in human pulmonary fibroblast leading to Ca^{2+} wave activity [23]. The IP_3 activation is the major Ca^{2+} release mechanism in fibroblast cells. When the legend bind to plasmalemma receptors, they cause the release of IP_3, which in term causes the release of sequestered Ca^{2+} and influx of extracellular Ca^{2+}. IP_3 receptor and $SERCA$ pump act as the source of Ca^{2+} from the ER which is used by the cell to initiate and sustain the signaling process required for smooth cellular functions.

Adenosine triphosphate (ATP) is an important signaling molecule that regulates various biological activities like increasing or reducing proliferation in various cells. Cardiac fibroblast cells are involved in maintaining structural, biochemistry, mechanical, and electrical characteristics of the heart [4]. ATP regulates the proliferation and migration of cardiac fibroblast cells. The cell migration was detected in a wound-healing assay. Cell proliferation increases with the increase in Ca^{2+} concentration. A significant effect of ATP at concentrations $0.1\mu M$ is observed in increasing the cell proliferation in cardiac fibroblast cells. But the extracellular ATP decreases cell proliferation in human cancer, endometrial stromal cells, respectively and neonatal fibroblast cells, the proliferation is reduced by extracellular ATP [19]. It stimulates cell growth in fibroblast cells. Approximately $1\mu M$ of ATP is present in the cell, and $1nM - 1\mu M$ is present outside the cell. ATP release and its metabolism dynamics regulate the intra and extracellular levels, which have a role in wound healing, contraction, relaxation, cell migration, differentiation, inflammation and cancer. Purinergic receptors (P_2Y) present on the cell membrane detect the ATP, thereby realizing IP_3 present in the membrane, and it is moved into the cytoplasm. The IP_3 then triggers the release of Ca^{2+} from the endoplasmic reticulum into the cytosol of the cell [19]. Therefore, it is of great interest to understand the functional aspects of Ca^{2+} signaling in a fibroblast cell [33].

A number of researchers have performed the study of Ca^{2+} distribution in various types of cells like neurons [13,43], astrocytes [12,41], myocytes [31,36,37], oocytes [24,28], acinar [20, 21], fibroblast [16], hepatocyte [11] cells, etc. Naik and Pardasani [25, 29] have studied a Ca^{2+} signaling in oocytes involving voltage-gated channel, buffer and RyR receptor. Harootunian et al. [7] explained the phenomena of oscillations in Ca^{2+} concentrations occurring due to the positive feedback between IP_3 and Ca^{2+} in a fibroblast cell. They proposed four classes of models of generating mechanisms. Van Zoelen et al. [47] clarified the major discrepancies between transformed and normal cells anchorage-independent growth (AIG) and loss of density-dependent growth inhibition ($DDGI$). In this investigation, they

used normal rate kidney (NRK) fibroblast cell, which has been used widely as a model system for examining the role played by growth factors in phenotype transformation.

Wagner and Keizer [48] analyzed the influence of buffer about Ca^{2+} release from internal stores. They also reported the effects of IP_3, rapid stationary and mobile Ca^{2+} buffers. Jafri and Keizer [9] analyzed the influence of Ca^{2+} diffusion in the cytosol, and Ca^{2+} handling by the ER on IP_3 affected Ca^{2+} wave propagation. Smith et al. [38] obtained an analytical solution to estimate the Ca^{2+} profile near the open Ca^{2+} channel for the steady-state condition of the transport equation proposed by Wagner and Keizer. Berridge et al. [2] reported that Ca^{2+} signaling in the cell triggers new life at fertilization control and controlling various development processes. Once the cells are differentiated, the Ca^{2+} functions to control processes like memory, secretion, proliferation, contraction and metabolism. They discussed the source of Ca^{2+}, elementary Ca^{2+} signals, the role of the endoplasmic reticulum or sarcoplasmic reticulum, IP_3 receptors and voltage-gated Ca^{2+} channel ($VGCC$) in Ca^{2+} signaling.

Godefridus and Harks [6] performed investigations on excitable fibroblasts, including ion channels, action potential and IP_3 signaling in NRK fibroblasts. Torres et al. [44] constructed a model for action potential generated in normal rate kidney fibroblasts. Kuster et al. [18] created a model for stabilizing the role of Ca^{2+}/IP_3 store-dependent plasma membrane and Ca^{2+}/IP_3 channels responsible for potential firing and intracellular Ca^{2+}/IP_3 fluctuations.

Chen et al. [4] investigated the mechanism of ATP regulates the proliferation of human cardiac fibroblast. Sun et al. [40] gave a dynamic model that provides a constitutive way for controlling the Ca^{2+} dynamics and the electrical field-induced intracellular Ca^{2+} response. Schmitz et al. [34] investigated the whole-cell Ca^{2+} dynamics using models of single trans-membrane ion-conducting proteins. They successfully described several experimental stages and captured important characteristics of Ca^{2+} dynamics upon T-cell receptor (TCR) stimulation. Hao and Rovin et al. [8] represented a mathematical progress model from tubulointerstitial inflammation into fibrosis, which can be used for monitoring the treatment for interstitial fibrosis in lupus nephritis autoimmune disease ($LNAD$). Also, they give a mathematical model of idiopathic pulmonary fibrosis. Lembong et al. [19] performed experiments in fibroblast cells under a variety of tissue conditions to study ATP. Kumar and Pardasani [17] developed a one-dimensional mathematical model for T-lymphocytes representing the intracellular Ca^{2+} distribution using a finite element approach. They also obtained the effect of source influx, buffers, and RyR receptor for exceptional cases and $SERCA$ pump for the temporal case.

Kotwani and Adlakha [16] constructed an excess buffer approximated model of the plasma membrane and endoplasmic reticulum Ca^{2+} influx and efflux in fibroblast cell. Jagtap and Adlakha [10] constructed a framework to observe the impact of fluxes and buffer on Ca^{2+} dynamics in a hepatocyte cell. Naik, Pardasani [26] studied the relationship of intracellular Ca^{2+} with RyR receptor, Na^{+}/Ca^{2+} exchanger, buffers, and $SERCA$ pump, in oocytes cell. Jagtap and Adlakha [10, 11] studied the distribution of intracellular calcium in the presence of buffers by using the finite elements method (FEM) in hepatocyte cells and concluded that calcium concentration decreases sharply for fast buffers, especially for endogenous and $BAPTA$ buffer in compression with exogenous ethylene glycol tetraacetic acid ($EGTA$) Buffer. Also, they studied the IP_3 and calcium association in hepatocyte cells involving $SERCA$ pump, ER leak, buffer, IP_3 diffusion and advection-diffusion of calcium. They concluded Ca^{2+} concentration increases due to the decrements in $SERCA$ pump rate constant, buffer concentration, and increment in advection velocity. Joshi and Jha [14] studied the fractional reaction-diffusion model for the one-dimensional case involving RyR, $VGCC$ and calbindin-D_{28k}, and they obtained analytical explanations for the physiology of Parkinson's brain. Martin Vaeth et al. [46] studied the effect of Ca^{2+} release-activated calcium ($CRAC$) channels and Stromal interacting molecule ($STIM$) in T cell-mediated

immunity calcium signaling. Joshi and Jha [15], using the fractional reaction-diffusion model, showed the complex interaction between calbindin-D_{28k} and Ca^{2+} in the presence of $VGCC$ in neuron cells. They used Fourier and Laplace transformation in the fractional form to deduce the solution for the Spatio-temporal fractional reaction-diffusion equation. Bazhutina et al. [1] propose a mathematical model of human cardiomyocytes to study the mechanical and electrical response with cardiac fibroblast cells to its electronic interaction.

No work is noticed for studying the influence of Ca^{2+} regulation on IP_3 and ATP production in a fibroblast cell. The attempt has been made in this direction in the paper.

2. MATHEMATICAL MODEL

The partial differential equation representing the one-dimensional Ca^{2+} dynamics in the presence of excess buffer and Ca^{2+} flux from the ER of the fibroblast cell is expressed below: [18, 44, 49]

$$\frac{\partial[Ca^{2+}]}{\partial t} = D_{Ca}\frac{\partial^2[Ca^{2+}]}{\partial x^2} - k_j^+[B]_\infty([Ca^{2+}] - [Ca^{2+}]_\infty) + \frac{A_{ER}}{V_{Cyt}}J_{ER}. \tag{2.1}$$

Here, $[B]_\infty$, $[Ca^{2+}]_\infty$ are the steady-state buffer and calcium concentration respectively. The diffusion coefficient of calcium is denoted by D_{Ca}. The position variable and time-variable are denoted by 'x' and 't,' respectively. The association rate of a buffer is denoted by k_j^+. The area of the endoplasmic reticulum and volume of the cytosol of the fibroblast cell is denoted by A_{ER} and V_{Cyt} respectively. The various influx and outflux terms of equation (2.1) can be written as [16]

$$J_{ER} = (J_{IP_3R} + J_{lkER} - J_{SERCA}). \tag{2.2}$$

$$J_{SERCA} = J_{SERCA}^{max}\frac{[Ca_{cyt}^{2+}]^2}{[Ca_{cyt}^{2+}]^2 + K_{SERCA}^2}, \tag{2.3}$$

$$J_{lkER} = K_{lkER}([Ca_{ER}^{2+}] - [Ca_{cyt}^{2+}]), \tag{2.4}$$

$$J_{IP_3R} = K_{IP_3R}([Ca_{ER}^{2+}] - [Ca_{cyt}^{2+}]). \tag{2.5}$$

To handle the nonlinearity in the equation (2.3), the following assumption [16] has been made. Let

$$K_{SERCA} >> [Ca_{cyt}^{2+}], \tag{2.6}$$

where K_{SERCA} denotes the calcium dissociation constant. Then we have,

$$\frac{[Ca_{cyt}^{2+}]}{[Ca_{cyt}^{2+}] + K_{SERCA}} << \frac{[Ca_{cyt}^{2+}]}{K_{SERCA}}. \tag{2.7}$$

Also,

$$\frac{[Ca_{cyt}^{2+}]^2}{[Ca_{cyt}^{2+}]^2 + K_{SERCA}^2} << \frac{[Ca_{cyt}^{2+}]}{K_{SERCA}^2} << \frac{[Ca_{cyt}^{2+}]}{K_{SERCA}}. \tag{2.8}$$

Substituting the values of equations (2.2) and (2.8) in (2.1), we get

$$\begin{aligned}\frac{\partial[Ca^{2+}]}{\partial t} &= D_{Ca}\frac{\partial^2[Ca^{2+}]}{\partial x^2} - k_j^+[B]_\infty([Ca^{2+}] - [Ca^{2+}]_\infty) + \\ &\frac{A_{ER}}{V_{cyt}}\left(K_{IP_3R}([Ca_{ER}^{2+}] - [Ca_{cyt}^{2+}]) + K_{lkER}([Ca_{ER}^{2+}] - [Ca_{cyt}^{2+}]) - \frac{J_{SERCA}^{mac}}{K_{SERCA}}[Ca_{cyt}^{2+}]\right).\end{aligned} \tag{2.9}$$

Calcium channels are presented on the ER membrane in fibroblast cells. In fibroblast cell intracellular calcium concentration is initially assumed at it's resting condition and it's value is $0.1\mu M$. Thus the initial condition is [27, 45],

$$[Ca^{2+}](x,0) = 0.1\mu M. \tag{2.10}$$

The boundary conditions for the cytosolic calcium at $x = 0$ and $x = 10$ are given by the following equations [16, 35]

$$\lim_{x\to 0}\left(-D_{Ca}\frac{\partial[Ca^{2+}]}{\partial x}\right) = \sigma_{Ca}, \tag{2.11}$$

where σ_{Ca} represents calcium flux on the left boundary of the fibroblast cell.

$$\lim_{x\to 10}[Ca^{2+}] = [Ca^{2+}]_{\infty} = 0.1\mu M. \tag{2.12}$$

The calcium-dependent ATP release are defined as [39]

$$ATP([Ca^{2+}]) = \left[\left(\frac{x_0}{x_0-1}\right) - 2\left(\frac{[Ca^{2+}]}{[Ca^{2+}]_{max}}\right)\right]\left[\left(\frac{1}{x_0-1}\right) - \left(\frac{[Ca^{2+}]}{[Ca^{2+}]_{max}}\right)^2\right]^{-1} \tag{2.13}$$

and the calcium-dependent IP_3 production is defined as [49]

$$IP_3([Ca^{2+}]) = V_{production}\left(\frac{[Ca^{2+}]^2}{[Ca^{2+}]^2 + K_{pump}^2}\right). \tag{2.14}$$

Here, x_0 is the constants for the ATP feedback and $[Ca^{2+}]_{max}$ considered as a maximum value of calcium concentration of the cell. Therefore, the set of equations (2.9), (2.10), (2.11) and (2.12) form an initial boundary value problem. The equation (2.9) is written as

$$\frac{1}{D_{Ca}}\frac{\partial[Ca^{2+}]}{\partial t} = \left(\frac{\partial^2[Ca^{2+}]}{\partial x^2}\right) - a_1[Ca^{2+}] + b_1, \tag{2.15}$$

where

$$a_1 = \frac{k_j^+[B]_{\infty}}{D_{Ca}} + \frac{1}{D_{Ca}F_c}\left(K_{IP_3R} + \frac{J_{SERCA}^{mac}}{K_{SERCA}} + V_{lkER}\right), \tag{2.16}$$

$$b_1 = \frac{k_j^+[B]_{\infty}}{D_{Ca}}[Ca^{2+}]_{\infty} + \frac{1}{D_{Ca}F_c}\left(K_{IP_3R}[Ca_{ER}^{2+}] + K_{lkER}[Ca_{ER}^{2+}]\right). \tag{2.17}$$

If we assume that the value of K_{SERCA} is very much less than the cytosolic calcium concentration. Then, the equation (2.15) is expressed as

$$\frac{\partial^2[Ca^{2+}]}{\partial x^2} - a_2[Ca^{2+}] + b_2 - \frac{1}{D_{Ca}}\frac{\partial[Ca^{2+}]}{\partial t} = 0, \tag{2.18}$$

where

$$a_2 = \frac{k_j^+[B]_{\infty}}{D_{Ca}} + \frac{1}{D_{Ca}F_c}\left(K_{IP_3R} + V_{lkER}\right), \tag{2.19}$$

$$b_2 = \frac{k_j^+[B]_{\infty}}{D_{Ca}}[Ca^{2+}]_{\infty} + \frac{1}{D_{Ca}F_c}\left(K_{IP_3R}[Ca_{ER}^{2+}] + K_{lkER}[Ca_{ER}^{2+}] - \frac{K_{SERCA}}{1+m^2}\right) \tag{2.20}$$

with F_c=$\dfrac{A_{ER}}{V_{cyt}}$ and $0 < m < 1$. From the equation (2.15) and equation (2.18), we get

$$\frac{\partial^2[Ca^{2+}]}{\partial x^2} - a[Ca^{2+}] + b - \frac{1}{D_{Ca}}\frac{\partial[Ca^{2+}]}{\partial t} = 0, \tag{2.21}$$

where $a = a_1$, $b = b_1$ for $K_{SERCA} >> [Ca^{2+}_{cyt}]$ and $a = a_2$, $b = b_2$ for $K_{SERCA} << [Ca^{2+}_{cyt}]$. The equation (2.21) is solved by using the finite elements method [30].

Here $'v'$ represent cytosolic calcium concentration. The equation (2.21) in discretized variational form is shown below:

$$J^{(el)} = \frac{1}{2}\int_{x_i^{(el)}}^{x_j^{(el)}} \left[\left(\frac{\partial v^{(el)}}{\partial x}\right)^2 + a(v^{(el)})^2 - 2bv^{(el)} + \frac{1}{D_c}\left(\frac{\partial v^{(el)}}{\partial t}\right)^2\right] dx - \mu^{(el)}\left(\frac{\sigma_{Ca}}{D_{Ca}} v^{(el)}\Big|_{x=0}\right). \tag{2.22}$$

Here, $el = 1, 2....10$. The constant term $\mu^{(el)} = 1.0$ for $el = 1.0$ and $\mu^{(el)} = 0.0$ for remaining elements.

3. SOLUTION

The linear interpolation function is employed for field variable in each element as given below:

$$v^{(el)} = c_1 + c_2 x, \tag{3.23}$$

where linear elements is denoted by 'el' and c_1, c_2 are constants. The equation (3.23) is written as

$$v^{(el)} = P^T C^{(el)}, \tag{3.24}$$

where $P^T = [1 \quad x]$, $C^{(el)} = \begin{bmatrix} c_1 \\ c_2 \end{bmatrix}$,

$$v^{(el)}(x_i) = c_1 + c_2 x_i = v_i, \tag{3.25}$$

$$v^{(el)}(x_j) = c_1 + c_2 x_j = v_j. \tag{3.26}$$

Using equations (3.24) - (3.26), we get:

$$\bar{v}^{(el)} = P^{(el)} C^{(el)}, \tag{3.27}$$

where $\bar{v}^{(el)} = \begin{bmatrix} v_i \\ v_j \end{bmatrix}$, $P^{(el)} = \begin{bmatrix} 1 & x_i \\ 1 & x_j \end{bmatrix}$,

$$C^{(el)} = (P^{(el)})^{-1} \bar{v}^{(el)}.$$

From equation (3.27), we have

$$C^{(el)} = R^{(el)} \bar{v}^{(el)}. \tag{3.28}$$

Thus,

$$R^{(el)} = (P^{(el)})^{-1} = \frac{1}{x_j - x_i}\begin{bmatrix} x_j & -x_i \\ -1 & 1 \end{bmatrix}.$$

From equation (3.24) and (3.28) we get

$$v^{(el)} = P^T R^{(el)} \bar{v}^{(el)} \tag{3.29}$$

and

$$v^{(el)'} = P_x^T R^{(el)} \bar{v}^{(e)}, \tag{3.30}$$

where $P_x^T = [0 \quad 1]$. Substituting the equations (3.29) and (3.30) in equation (2.22) we get

$$\begin{aligned} J^{(el)} = \frac{1}{2} \int_{x_i{}^{(el)}}^{x_j{}^{(el)}} \Bigg(& (P_x^T R^{(el)} \bar{v}^{(el)})^2 + a(P^T R^{(el)} \bar{v}^{(el)})^2 - 2bP^T R^{(el)} \bar{v}^{(el)} + \\ & \frac{1}{D_c} \frac{\partial (P^T R^{(el)} \bar{v}^{(el)})^2}{\partial t} \Bigg) dx - \mu^{(el)} \left(\frac{\sigma_{Ca}}{D_{Ca}} P^T R^{(el)} \bar{v}^{(el)}|_{x=0} \right). \end{aligned} \tag{3.31}$$

$$\begin{aligned} \frac{\partial J^{(el)}}{\partial \bar{v}^{(el)}} = \int_{x_i{}^{(el)}}^{x_j{}^{(el)}} & ({R^{(el)}}^T P_x P_x^T R^{(el)} \bar{v}^{(el)}) + a({R^{(el)}}^T P P^T R^{(el)} \bar{v}^{(el)}) - b({R^{(el)}}^T P) \\ & + \frac{1}{D_c} \frac{\partial (P^T R^{(el)} \bar{v}^{(el)})}{\partial t} dx - \mu^{(el)} \left(\frac{\sigma_{Ca}}{D_{Ca}} P^T R^{(el)} \bar{v}^{(el)}|_{x=0} \right). \end{aligned} \tag{3.32}$$

We can write equation (3.32) as

$$\frac{\partial J^{(el)}}{\partial \bar{v}^{(el)}} = \frac{\partial J_1^{(el)}}{\partial \bar{v}^{(el)}} + \frac{\partial J_2^{(el)}}{\partial \bar{v}^{(el)}} - \frac{\partial J_3^{(el)}}{\partial \bar{v}^{(el)}} + \frac{\partial J_4^{(el)}}{\partial \bar{v}^{(el)}} - \frac{\partial J_5^{(el)}}{\partial \bar{v}^{(el)}}, \tag{3.33}$$

where

$$\frac{\partial J_1^{(el)}}{\partial \bar{v}^{(el)}} = \int_{x_i{}^{(el)}}^{x_j{}^{(el)}} ({R^{(el)}}^T P_x P_x^T R^{(el)} \bar{v}^{(el)}) dx, \tag{3.34}$$

$$\frac{\partial J_2^{(el)}}{\partial \bar{v}^{(el)}} = a \int_{x_i{}^{(el)}}^{x_j{}^{(el)}} ({R^{(el)}}^T P P^T R^{(el)} \bar{v}^{(el)}) dx, \tag{3.35}$$

$$\frac{\partial J_3^{(el)}}{\partial \bar{v}^{(el)}} = b \int_{x_i{}^{(el)}}^{x_j{}^{(el)}} ({R^{(el)}}^T P) dx, \tag{3.36}$$

$$\frac{\partial J_4^{(el)}}{\partial \bar{v}^{(el)}} = \frac{1}{D_c} \int_{x_i{}^{(el)}}^{x_j{}^{(el)}} \left(\frac{\partial (P^T R^{(el)} \bar{v}^{(el)})}{\partial t} \right) dx,$$

$$\frac{\partial J_5^{(el)}}{\partial \bar{v}^{(el)}} = \mu^{el} \left(\frac{\sigma_{Ca}}{D_{Ca}} {R^{(el)}}^T P|_{x=0} \right).$$

Now the integral $J^{(el)}$ is minimized with respect to each nodal points as shown below:

$$\frac{\partial I^{(el)}}{\partial \bar{v}^{(el)}} = 0, \tag{3.37}$$

$$\frac{\partial J^{(el)}}{\partial \bar{v}^{(el)}} = \frac{\partial J_1^{(el)}}{\partial \bar{v}^{(el)}} + \frac{\partial J_2^{(el)}}{\partial \bar{v}^{(el)}} - \frac{\partial J_3^{(el)}}{\partial \bar{v}^{(el)}} + \frac{\partial J_4^{(el)}}{\partial \bar{v}^{(el)}} - \frac{\partial J_5^{(el)}}{\partial \bar{v}^{(el)}} = 0, \tag{3.38}$$

$$\frac{\partial J}{\partial \bar{v}} = \Sigma \bar{M}^{(el)} \frac{\partial J^{(el)}}{d\bar{v}^{(el)}} \bar{M}^{(el)^T} = 0, \tag{3.39}$$

where $\overline{M}^{(el)} = \begin{bmatrix} 0 & 0 \\ . & . \\ 1 & 0 \\ 0 & 1 \\ . & . \\ 0 & 0 \end{bmatrix}$, $\overline{u} = \begin{bmatrix} v_1 \\ v_2 \\ . \\ . \\ . \\ v_{11} \end{bmatrix}$.

Assembling the integral equations (3.39) we get

$$J = \Sigma J^{(el)}. \tag{3.40}$$

The equations (3.39) and (3.40) lead to the following system of linear differential equations

$$[P]_{11\times 11} \left[\frac{\partial \bar{u}}{\partial t}\right]_{11\times 1} + [Q]_{11\times 11}[\bar{u}]_{11\times 1} = [R]_{11\times 1}. \tag{3.41}$$

Here, $[\bar{v}] = [v_1, v_2, v_3, ..., .v_{11}]$, P is a system matrix, Q is the system vector and R is a force vector. The Crank Nicholson method is use for solving the system (3.41). Matlab has been used to simulate the problem and obtain numerical results.

4. RESULTS AND DISCUSSION

The biophysical values and numerical constants used in computing the numerical results are shown in Table 4.2.

Fig. 4.1 displays the spatial and temporal Ca^{2+}, ATP, and IP_3 concentration profiles for various values of time and positions. From fig. 4.1(A), it is clear that spatial Ca^{2+} concentration continuously decreases at each nodal point in the cytosol of the fibroblast cell with the increased distance from the source. This is due to the presence of source flux at $x = 0.0\mu m$ and the diffusion of Ca^{2+} towards $x = 10\mu m$. In fig. 4.1(B), it is notice that the Ca^{2+} concentration is $0.1\mu M$ at $t = 0msec$ and increases with increases in time. The rise in calcium concentration at the node at $x = 0\mu m$ is more than other points and becomes lower as we move from $x = 0\mu m$ to $x = 10\mu m$. It achieves a steady-state in time $t = 150msec$. Fig. 4.1(C, D) displays the calcium-dependent ATP production in space and time. It is evident from fig. 4.1(C) at the initial node, the concentration of ATP is higher and decreases gradually towards the ending node. From fig. 4.1(D), it is clear that the range of ATP varies from a lower concentration of $0.4\mu M$ to a higher concentration of $1\mu M$, which depends on calcium concentration, in this case, when the initial concentration of calcium is $0.1\mu M$ then the ATP is $0.4\mu M$. Therefore calcium and ATP are directly proportional and converge to a steady-state in time $t = 150msec$.

Fig. 4.1(E, F) shows the calcium-dependent IP_3 production for space and time. The concentration of IP_3 is higher at the mouth of source influx. It decreases gradually on moving far from the source, and later it converges to the 0.005 μM. In fig. 4.1(F) it is notice that IP_3 concentration is $0.005\mu M$ at $t = 0msec$ and increases with an increase in time. The rise in IP_3 concentration is more at x=0 μm and becomes lower as we move from $x = 0\mu m$ to $x = 10\mu m$. It achieves a steady-state in time at $150msec$. Therefore, it is clear that the IP_3 production and Ca^{2+} concentration show similar behavior.

Fig. 4.2 shows the profile of spatial and temporal Ca^{2+}, ATP, and IP_3 concentration for the different values of source amplitude along with the concentration of buffer $5\mu M$ and the value of diffusion coefficient $250\mu m^2/s$. In fig. 4.2, it is notice that the concentration of Ca^{2+}, ATP, and IP_3 is more for higher values of source amplitude. In fig. 4.2(A, C, E)

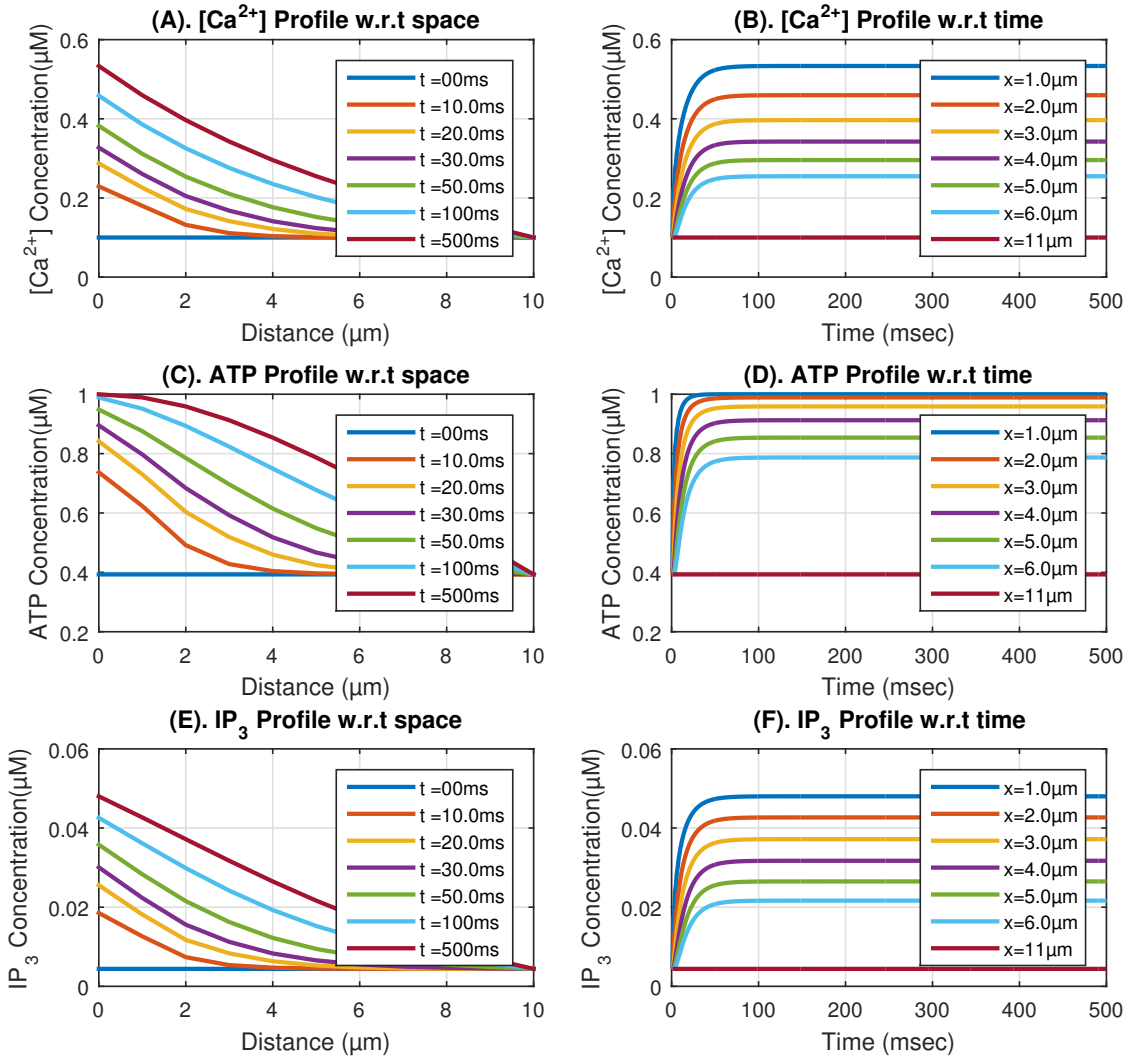

Fig. 4.1. Calcium, ATP and IP_3 concentration profile in a fibroblast cell at various time and positions for $[B] = 5\mu M$, $D_c = 250\mu m^2/s$ and $\sigma = 20pA$.

the calcium, ATP, and IP_3 concentration is higher at the source $x = 0\mu m$ and decreases along the spatial direction and converges to $0.1\mu M$, $0.25\mu M$ and $0.005\mu M$ at $x = 10.0\mu m$ respectively. From fig. 4.2(B, D, F) it is clear that the calcium, ATP, and IP_3 concentration achieves a steady-state in time $t = 180msec$. Therefore calcium, ATP, IP_3 are dependent on the source amplitude.

Fig. 4.3 displays the spatial and temporal calcium, ATP, and IP_3 concentration for the various values of association rate of the buffer in the fibroblast cell. From fig. 4.3(A, C, E), it is noticed that as buffer binding rate increases calcium, ATP and IP_3 concentration decreases. From fig. 4.3(B, D, F) it is clear that the calcium, ATP, and IP_3 dynamics achieves a steady-state in time $t = 175msec$. Therefore calcium, ATP, IP_3 are reliant on the association rate of the buffer in the fibroblast cell.

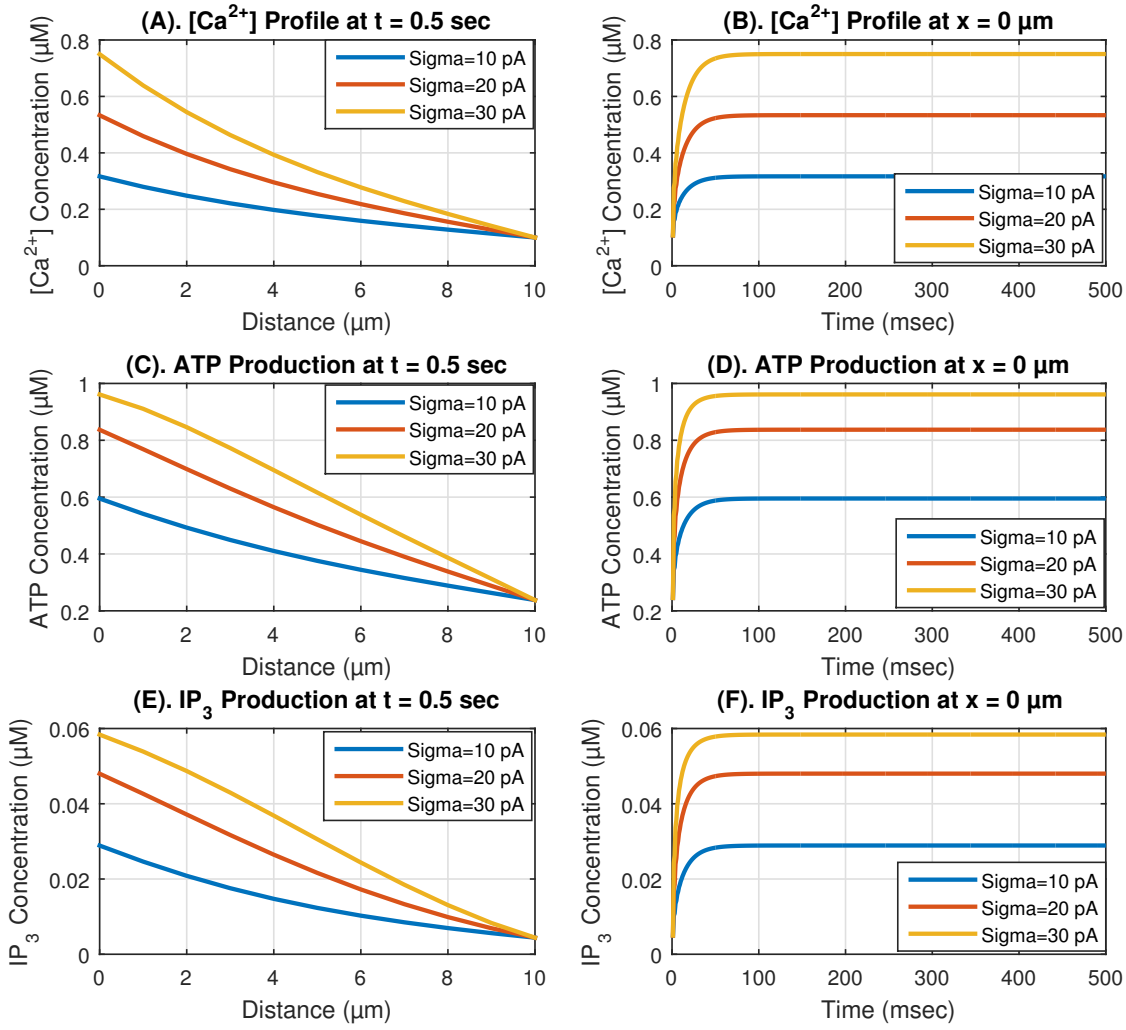

Fig. 4.2. Ca^{2+}-dependent ATP and IP_3 concentration profile in fibroblast cell for different source influx for $[B] = 5\mu M$ and $D_c = 250\mu m^2/s$.

Fig. 4.4 shows the differences in spatial and temporal calcium, ATP and IP_3 concentration for the different values of diffusion coefficient i.e $220\mu m^2/s$, $270\mu m^2/s$, $320\mu m^2/s$. From fig. 4.4(A, C, E) it is notice that for the higher value of diffusion coefficient calcium, ATP, and IP_3 ion move fast from apical to the basal region of the cell. Therefore, the concentration of calcium, ATP, and IP_3 decreases with an increase in the value of diffusion coefficient near the source and calcium concentration uniformly converges to $0.1\mu M$. ATP concentration and IP_3 concentration converges to $0.22\mu M$ and $0.005\mu M$ respectively. The fig. 4.4(A, B) it is observed that calcium concentration is $0.58\mu M$, $0.51\mu M$, and $0.47\mu M$ for the diffusion coefficient $220\mu m^2/s$, $270\mu m^2/s$, $320\mu m^2/s$. Therefore diffusion and calcium concentration is inversely proportional to each other. In fig. 4.4(C, D, E, F) concentration of ATP and IP_3 are inversely proportional to the value of diffusion coefficient and achieve a steady-state in time $t = 125msec$.

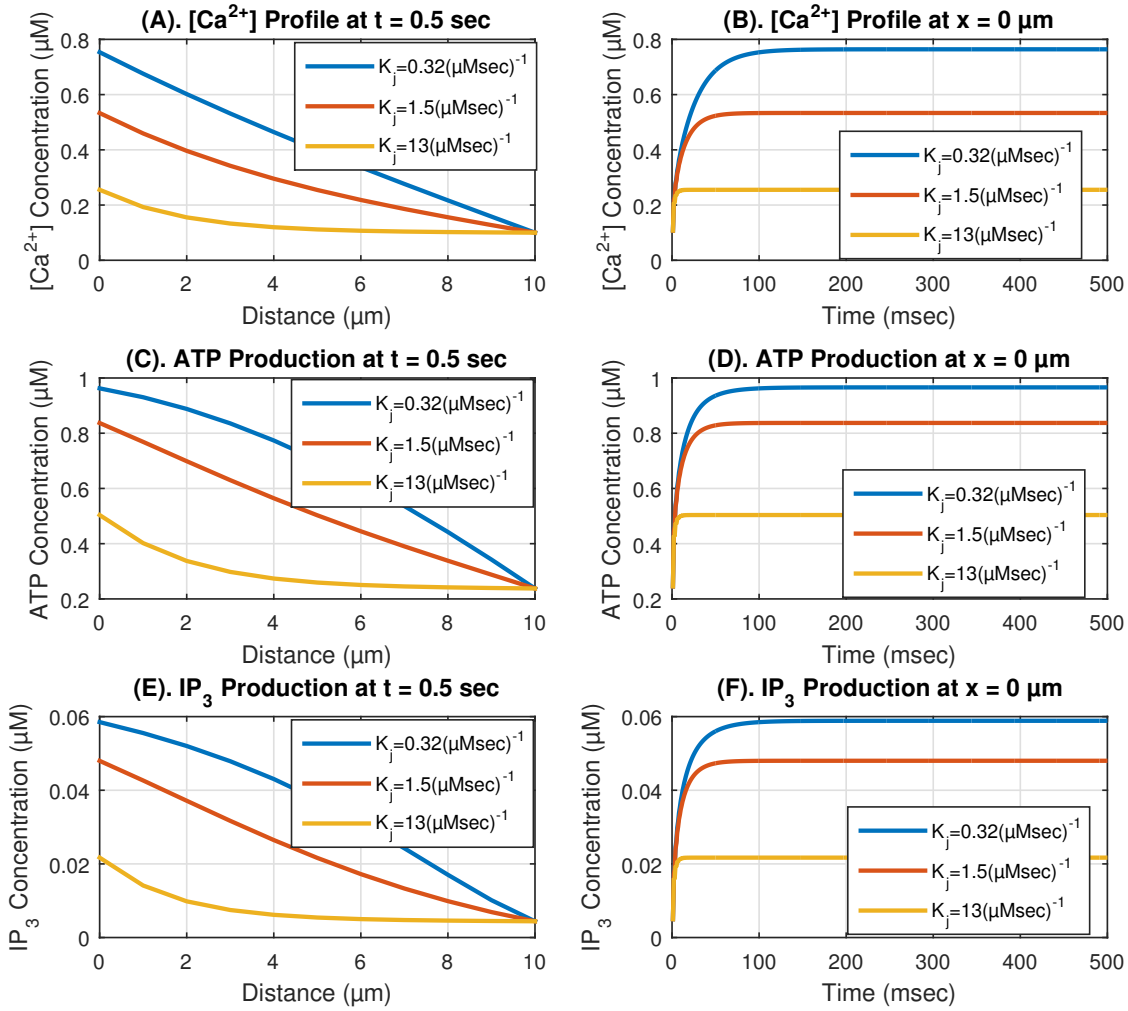

Fig. 4.3. Ca^{2+}-dependent ATP and IP_3 concentration profile in fibroblast cell for different calcium binding association rate for $[B] = 5\mu M$, $D_c = 250\mu m^2/s$ and $\sigma = 20pA$.

Fig. 4.5 displays the spatial and temporal distribution of Ca^{2+}, ATP, and IP_3 concentration for the different values of ethylene glycol tetraacetic acid ($EGTA$) buffers. From fig. 4.5, it is clear that the concentration of free Ca^{2+}, ATP, and IP_3 decreases at each nodal point of a fibroblast cell with the increase in the concentration of $EGTA$ buffers $5\mu M$, $10\mu M$ and $15\mu M$. This $EGTA$ binds with free Ca^{2+} makes a calcium-bound buffer in the cytosol and reduces the amount of free Ca^{2+}. Thus, the increase in the concentration of buffer causes a decrease in the free Ca^{2+} concentration. The rate of decrease in Ca^{2+} concentration increases with the rise in $EGTA$ buffer concentration. The Ca^{2+} concentration uniformly decreases towards the basal part of the fibroblast cell and attains a background equilibrium concentration of $0.1\mu M$. It is clear from the results of fig. 4.1 and fig. 4.5 the behavior of calcium profiles are followed by the ATP and IP_3 profiles. Ca^{2+}, ATP, and IP_3 concentrations are inversely proportional to buffer binding affinity.

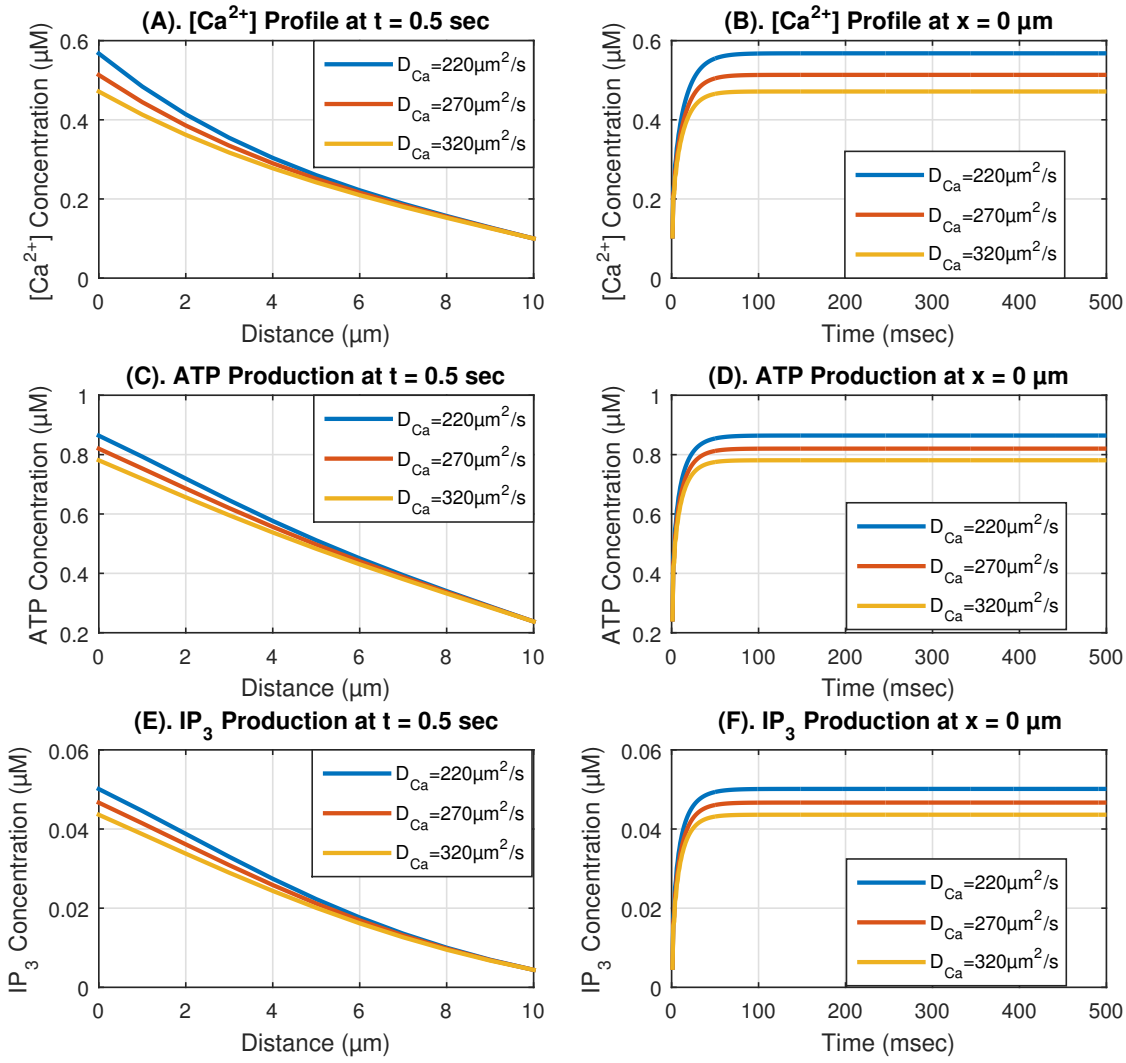

Fig. 4.4. Calcium, ATP and IP_3 concentration profile in a fibroblast cell for the different values of diffusion coefficient at $[B] = 5\mu M$ and $\sigma = 20pA$.

The ratio of calcium and ATP in fig. 4.6(A) is highest at the calcium source and lowest along the spatial direction and became constant at the other end. They were comparing the fig. 4.6(A, B) with the calcium and ATP profiles of fig. 4.1, it shows that the sharpness of the curves in calcium and ATP profile in fig. 4.1 has got reduced in this fig. 4.6. This shows that the behavior of calcium and ATP is very close. In fig. 4.6(B), the ratio of calcium and ATP is lowest at time $t = 0msec$ and increases with time and achieves a steady-state in $110msec$. The steady-state time in fig. 4.6(B) is less in fig. 4.1(B, D) for the calcium and ATP. This shows that the temporal profile of calcium and ATP behavior is very close to each other. In fig. 4.6(C), the spatial profile of the ratio of calcium and IP_3 is different from that in fig. 4.1 for calcium and IP_3 profiles. For $t = 25msec$ the special profile of calcium and IP_3 ratio is increasing concave whereas for $t = 500msec$ this ratio profile is increasing convex from $x = 0\mu m$ to $x = 10\mu m$.

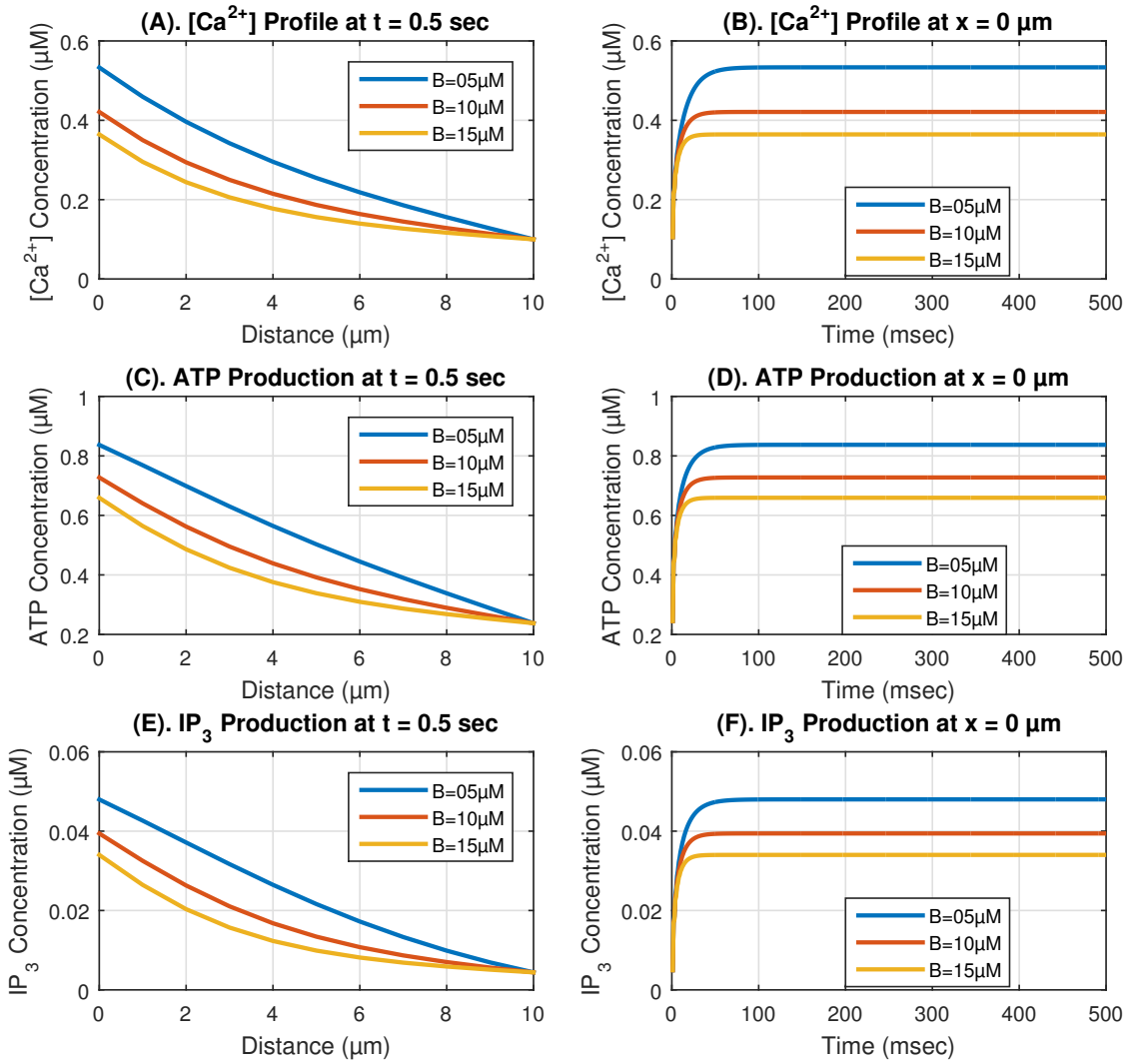

Fig. 4.5. Calcium, ATP and IP_3 concentration profile in a fibroblast cell for the different values of buffer for $D_c = 250\mu m^2/s$ and $\sigma = 20pA$.

The calcium profile in fig. 4.1 is decreasing convex. The IP_3 profiles in fig. 4.1 are also decreasing convex for $t = 25msec$ and $50msec$. But for $t = 500msec$ the IP_3 profile was decreasing concave. The drastic change in the ratio of calcium and IP_3 profiles indicates a significant difference in the behavior of calcium and IP_3 profiles. In fig. 4.6(D), the temporal profile ratio of calcium and IP_3 is almost similar for $x = 3\mu m$ and $x = 6\mu m$ in behavior. Still, there is a change in behavior at $x = 1\mu m$ compared to calcium and IP_3 profiles in fig. 4.1 This shows that the behavior of curves of calcium and IP_3 is very close at all spatial points for $x > 1\mu m$ in fig. 4.1 but is different near the source. These fluctuations are due to a mismatch in calcium and IP_3 profile near the source. The steady-state time of the ratio of calcium and IP_3 profiles is less than the independent calcium and IP_3 profiles.

Fig. 4.7 shows the influence of calcium on the spatial and temporal flux of IP_3 degradation profile in a fibroblast cell. The maximum concentration of degradation is observed at

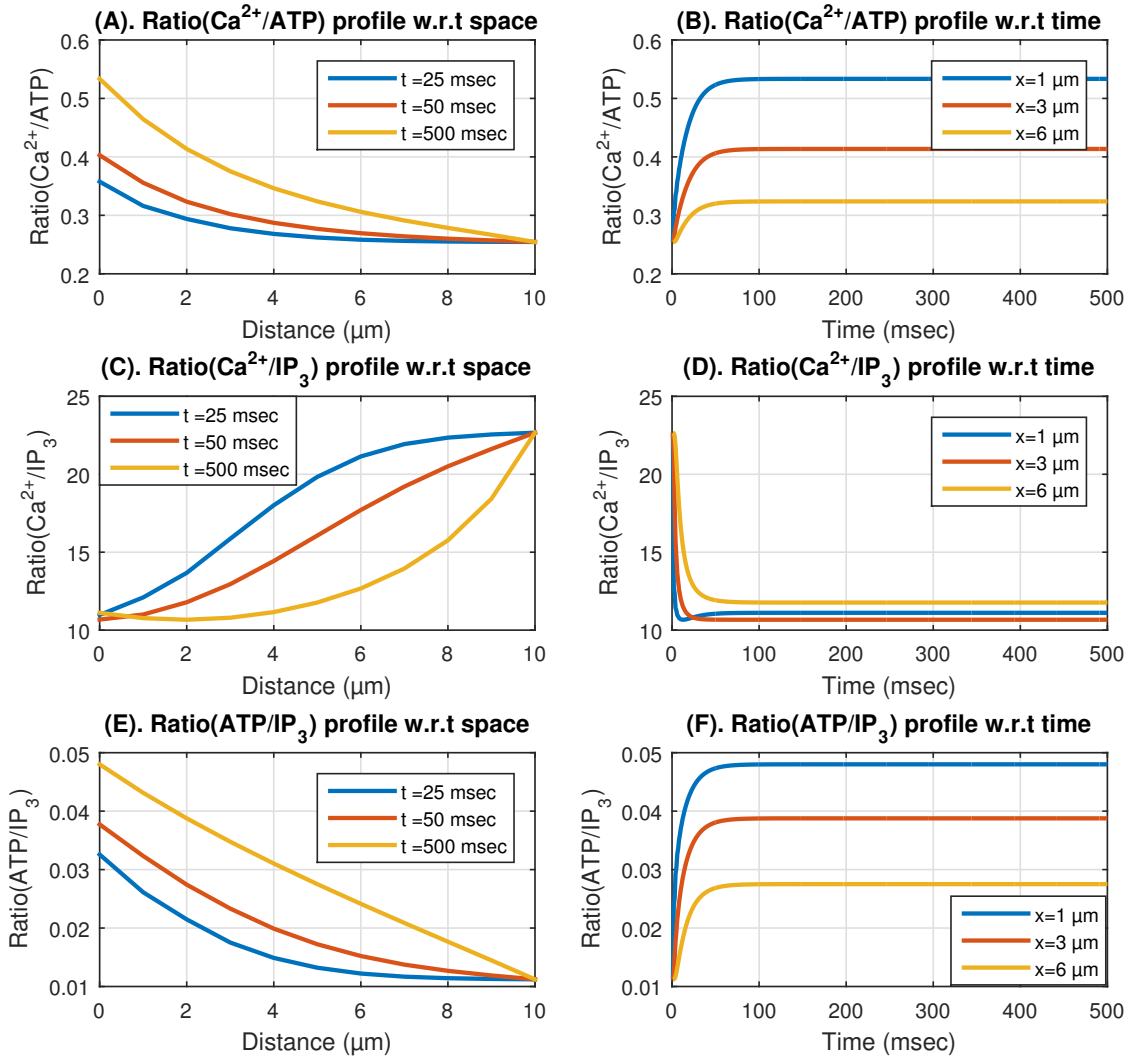

Fig. 4.6. Ratio of Ca^{2+}-dependent ATP and IP_3 with the calcium for different points of time and position for $[B] = 5\mu M$, $D_c = 250\mu m^2/s$ and $\sigma = 20pA$.

$x = 0.0\mu m$ and it reduces from $x = 0.0\mu m$ to $x = 10.0\mu m$. In fig. 4.7, it is clear that the high value of calcium leads to the higher degradation of IP_3. Further, it shows that IP_3 concentration becomes low due to higher degradation of IP_3.

Fig. 4.8 shows the ratio of calcium, ATP, and IP_3 concentrations for various values of source amplitude. It is noticed in fig. 4.8(A) that the peak value of calcium ratio for sigma $10pA$ and $20pA$ is 1.68 at $x = 0\mu m$. The peak value of ATP and IP_3 ratios are notice at $x = 1\mu m$ and $x = 3\mu m$ respectively. At the initial node, calcium concentration is 68 percent higher than the ATP and lower than the IP_3 percentage ratio, which is 81 percent. The minimum ratio is attained at the last node. In fig. 4.8(B) the ratio profile of calcium, ATP and IP_3 for sigma $10pA$ and $20pA$ is minimum at time $t = 0msec$ and increases with time from $t = 0msec$ to $t = 15msec$ for ATP and IP_3. The calcium ratio gradually increases with

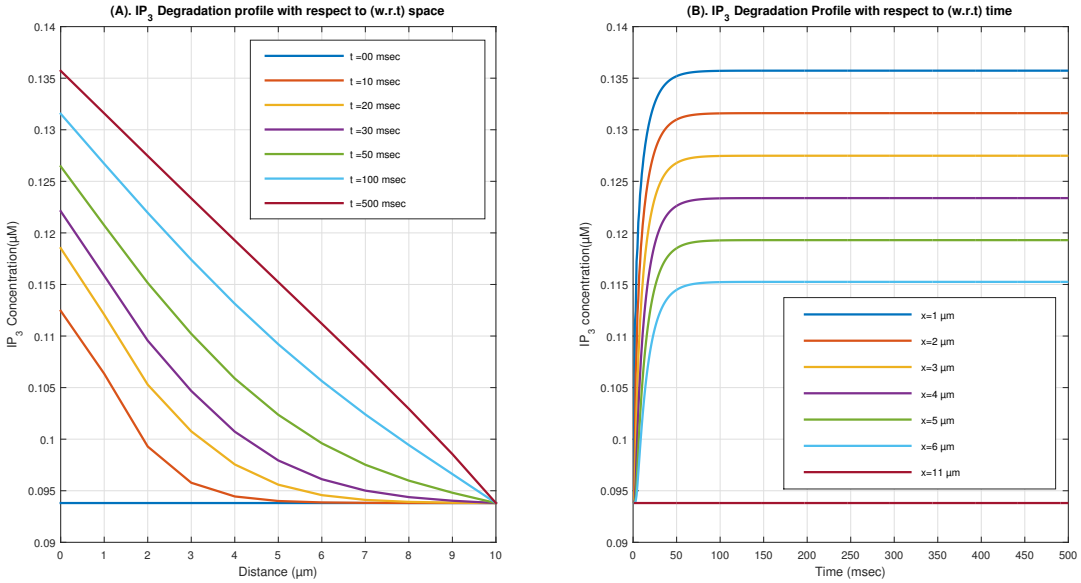

Fig. 4.7. $[Ca^{2+}]$-dependent IP_3 degradation for different points of time and position for $[B] = 5\mu M$, $D_c = 250\mu m^2/s$ and $\sigma = 20pA$.

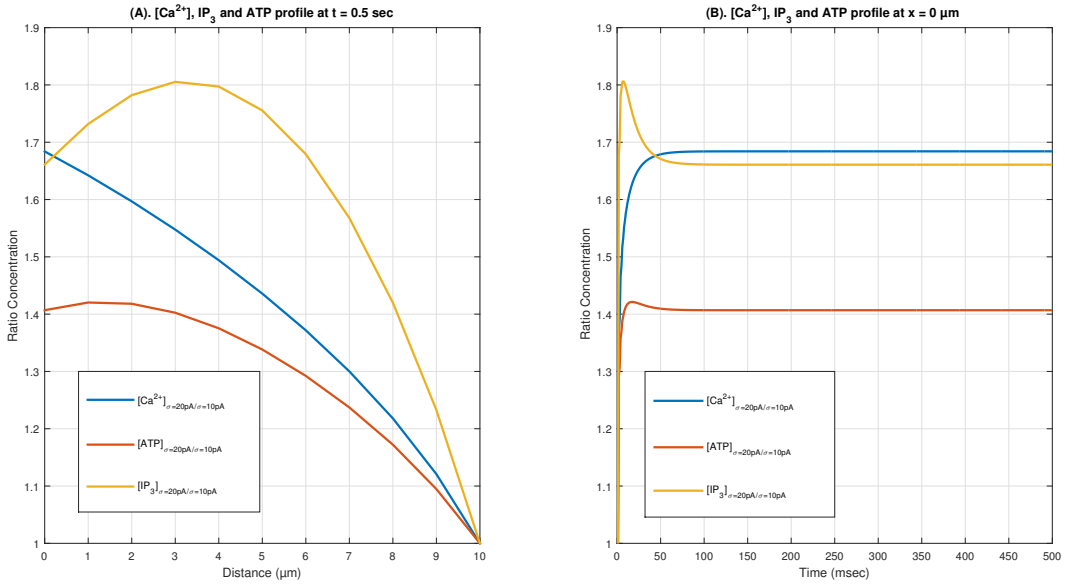

Fig. 4.8. Ratio of Calcium, ATP and IP_3 for different source influx for $[B] = 5\mu M$ and $D_c = 250\mu m^2/s$.

time and achieves a steady-state in $90msec$, ATP, and IP_3 ratios for sigma $10pA$ and sigma $20pA$ also achieve steady state in $90msec$.

Fig. 4.9 shows the ratio graph of calcium, ATP, and IP_3 concentrations for different values of the buffer. It is observed in fig. 4.9(A) that the peak value of calcium, ATP and IP_3 ratios are at $4\mu m$ and $5\mu m$ respectively. Initial node calcium concentration is 26%, which is higher for buffer $5\mu M$ and $10\mu M$ than the ATP and IP_3 ratio percentage. The minimum ratio is attained at the last node. In fig. 4.9(B), the ratio profile of calcium, ATP, and IP_3 is

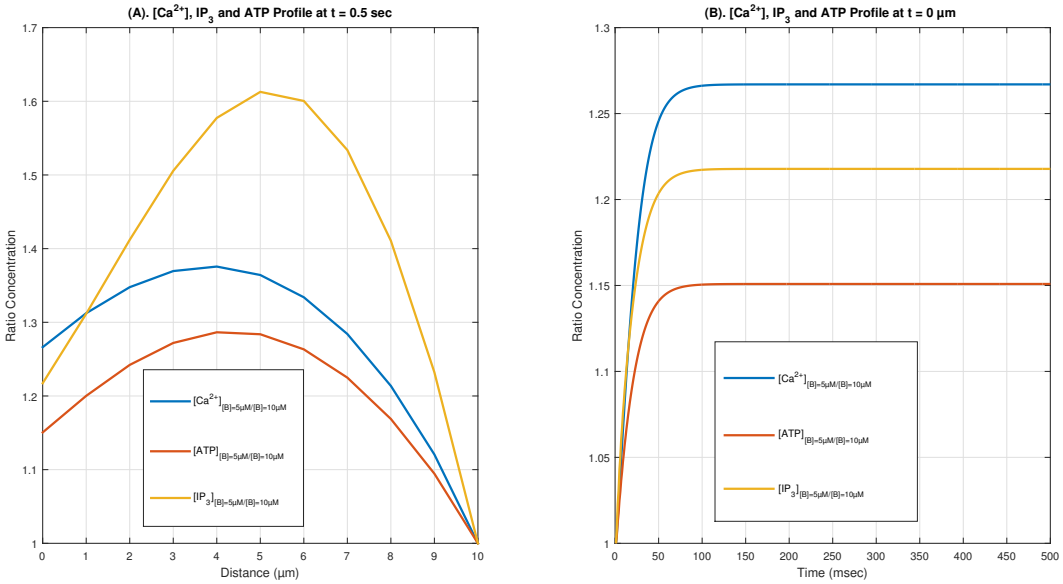

Fig. 4.9. Ratio of Calcium, ATP and IP_3 for different buffers for $D_c = 250\mu m^2/s$ and $\sigma = 20pA$.

Table 4.1. Steady state time period for the Ca^{2+}, IP_3 and ATP

Fig. No.	Temporal Profile	Time required to achieve steady state
1-B	Calcium w.r.t time	$150msec$
1-D	ATP w.r.t time	$150msec$
1-F	IP_3 w.r.t time	$150msec$
2-B	Calcium at $x = 0$	$180msec$
2-D	ATP at $x = 0$	$180msec$
2-F	IP_3 at $x = 0$	$180msec$
3-B	Calcium at $x = 0$	$175msec$
3-D	ATP at $x = 0$	$175msec$
3-F	IP_3 at $x = 0$	$175msec$
4-B	Calcium	$125msec$
4-D	ATP	$115msec$
4-F	IP_3	$100msec$
5-B	Calcium	$90msec$
5-D	ATP	$95msec$
5-F	IP_3	$100msec$
6-B	Ratio Calcium/ATP	$110msec$
6-D	Ratio Calcium/ IP_3	$100msec$
6-F	Ratio ATP / IP_3	$105msec$
7	IP_3 degradation	$150msec$
8	Ratio of Calcium, ATP, IP_3	$90msec$
9	Ratio of Calcium, ATP, IP_3	$100msec$

lowest at time $t = 0msec$ and increases with time and achieves a steady-state in $100msec$ for buffer $5\mu M$ and $10\mu M$.

In Figures 4.1 to 4.9 the profiles of calcium, IP_3 and ATP are observed to be nonlinear which implies that the nonlinear phenomena is occurring due to changes in conditions like alteration in values of buffer, source influx, etc. to balance the effects of these alterations in parameters for regulating the concentrations of calcium, IP_3 and ATP at appropriate levels to maintain the structure and function of the cell.

Table 4.2. List of physiological parameters [44]

Symbol	Parameters	Values
$[Ca^{2+}]_\infty$	Background calcium concentration	0.1 μm
J^{max}_{SERCA}	Maximal pump rate of $SERCA$	$8{\times}10^{-5}\frac{\mu mol}{(s \times dm^2)}$
K_{SERCA}	$SERCA$ calcium dissociation constant	$2.0\mu m$
K_{lkER}	Leak constant	$2.0s^{-1}$
$[Ca^{2+}]_{ER}$	ER calcium concentration	10.89 μm
A_{ER}	ER area	$0.3 \times 10^{-7} dm^2$
V_{ER}	Volume of ER	$0.1 \times 10^{-12} dm^3$
V_{cyt}	Volume of cytosol	$1 \times 10^{-12} dm^3$
K_j^+	Association rate	$1.5(mms)^{-1}$
$[B]_\infty$	Total buffer concentration	20 μm
σ	Source amplitude	15pA
D_{Ca}	Diffusion coefficient	$250\mu m^2/s$

Table 4.3. Error analysis of $[Ca^{2+}]$ concentration profile at $x = 0\mu m$

Time	N=10 elements	N=20 elements	Error	Error %
$t = 100msec$	0.7535093547	0.889250659	0.13574	0.15264 %
$t = 200msec$	0.7638349682	0.994152451	0.23031	0.23165%
$t = 300msec$	0.7640457957	1.015927426	0.25188	0.24794 %
$t = 500msec$	0.7640501883	1.021388902	0.25739	0.25195 %
$t = 1000msec$	0.7640501901	1.021634989	0.25758	0.25212%

Table 4.4. Error analysis of ATP production profile at $x = 1\mu m$

Time	N=10 elements	N=20 elements	Error	Error %
$t = 100msec$	0.9892130695	0.918883410	0.07032	0.07653 %
$t = 200msec$	0.9893086343	0.870996603	0.11831	0.13583%
$t = 300msec$	0.9893087359	0.860896109	0.12841	0.14916 %
$t = 500msec$	0.9893087360	0.858363403	0.13094	0.15255 %
$t = 1000msec$	0.9893087361	0.858249304	0.13106	0.15270%

Table 4.5. Error analysis of IP_3 production profile at $x = 2\mu m$

Time	N=10 elements	N=20 elements	Error	Error %
$t = 100msec$	0.0371489218	0.058113011	0.020964	0.36075 %
$t = 200msec$	0.0371770587	0.0612872185	0.024112	0.39341%
$t = 300msec$	0.0371770887	0.0618411302	0.024664	0.39883 %
$t = 500msec$	0.0371770888	0.0619751619	0.024798	0.40013 %
$t = 1000msec$	0.0371770888	0.0619811563	0.024804	0.40019%

For the time period $t = 100$, 200, 300, 500 and 1000 $msec$, the accuracy of the model for calcium are 99.84736 %, 99.76835 %, 99.975206 %, 99.74805 % and 99.74788 %, respectively, and for ATP production, the accuracy is 99.92347 %, 99.86417 %, 99.85084 %, 99.84745 % and 99.8473 %, respectively. For IP_3 production, the accuracy is 99.63925 %, 99.60659 %, 99.60117 %, 99.59987 %, and 99.59981 %, respectively. Thus the minimum accuracy and maximum error % for this model are 99.75 % and 0.40 %, respectively. The grid sensitivity is negligible; this implies that the solution is independent of the grid. To perform stability analysis, calculated the spectral radius, and the system is said to be stable if the spectral radius is less than or equal to unity [50]. In this case, the spectral radius was 0.9619, which is less than unity. Thus the finite element solution in the present condition is stable.

5. CONCLUSION

A one-dimensional model is proposed to investigate the impact of buffer, channel flux, and diffusion coefficient on spatial and temporal calcium profile in fibroblast cells and study their impact on ATP and IP_3 production in the cell. It is concluded that spatial and temporal calcium distribution variation is proportional to the source influx and inversely proportional to diffusion coefficient and buffers. The variation in spatial and temporal profiles of ATP and IP_3 production is also directly proportional to source influx and inversely proportional to buffer and diffusion coefficient. The IP_3 degradation is also proportional to calcium distribution in the cell. The finite element simulation is quite effective in generating these insights, which may help frame measures for diagnosis and treatment. The outcomes of this study are in agreement with biological facts. The non-availability of the experimental results for the conditions of the present problem is constant, preventing validation impossible.

The dysregulation effect of source influx, buffers, and diffusion coefficients calcium profiles are transferred to the ATP, IP_3 production, and IP_3 degradation profiles. Thus the changes in source influx, buffers, and diffusion coefficient can cause an increase or decrease in ATP and IP_3 production and IP_3 degradation. The IP_3 is involved in the function of the $SERCA$ pump. Therefore causes alteration in calcium profile due to the $SERCA$ pump leading to dysregulation in calcium dynamics. The variation in ATP can cause changes in differentiation, contraction, relaxation, migration, wound healing, etc. Here the dysregulation of ATP can lead to severe disorders such as inflammation, heart disease, and cancer. The results from our model here give us an insight into the parameters which may help regulate serious disorders such as cancer, inflammation, and heart disease.

REFERENCES

1. Bazhutina, A., Balakina-Vikulova, N. A., Kursanov, A., Solovyova, O., Panfilov, A. et. al. (2021). Mathematical modelling of the mechano-electric coupling in the human cardiomyocyte electrically connected with fibroblasts. *Progress in Biophysics and Molecular Biology*, **159**, 46–57.
2. Berridge, M., Lipp, P. & Bootman, M. (1999). Calcium signalling. *Current biology*, **9**(5), 157–159.
3. Carafoli, E. (2002). Calcium signaling: a tale for all seasons. *Proceedings of the National Academy of Sciences*, **99**(3), 1115–1122.
4. Chen, J. B., Liu, W. J., Che, H., Liu, J., Sun, H. Y. et. al. (2012). Adenosine-5-triphosphate up-regulates proliferation of human cardiac fibroblasts. *British journal of pharmacology*, **166**(3), 1140–1150.
5. Chen, J. B., Tao, R., Sun, H. Y., Tse, H. F., Lau, C. P. et. al. (2010). Multiple Ca^{2+} signaling pathways regulate intracellular Ca^{2+} activity in human cardiac fibroblasts. *Journal of cellular physiology*, **223**(1), 68–75.
6. Harks, E.G., Torres, J.J., Cornelisse L.N., Ypey D.L. & Theuvenet A.P. (2003). Ionic basis for excitability in normal rat kidney (NRK) fibroblasts. *J Cell Physiol*, **196**, 493–503.
7. Harootunian, A. T., Kao, J. P., Paranjape, S. & Tsien, R. Y. (1991). Generation of calcium oscillations in fibroblasts by positive feedback between calcium and IP_3. *Science*, **251**(4989), 75–78.
8. Hao, W., Rovin, B. H. & Friedman, A. (2014). Mathematical model of renal interstitial fibrosis. *Proceedings of the National Academy of Sciences*, **111**(39), 14193–14198.
9. Jafri, M. S. & Keizer, J. (1995). On the roles of Ca^{2+} diffusion, Ca^{2+} buffers, $\&$ the endoplasmic reticulum in IP_3-induced Ca^{2+} waves. *Biophysical journal*, **69**(5), 2139–2153.
10. Jagtap, Y. & Adlakha, N. (2018). Finite volume simulation of two dimensional calcium dynamics in a hepatocyte cell involving buffers and fluxes. *Commun Math Biol Neurosci*, **15**, 1–16.
11. Jagtap, Y. & Adlakha, N. (2019). Numerical study of one-dimensional buffered advection–diffusion of calcium & IP_3 in a hepatocyte cell. *Network Modeling Analysis in Health Informatics and Bioinformatics*, **8**(1), 1–9.
12. Jha, B. K., Adlakha, N. & Mehta, M. N. (2014). Two-dimensional finite element model to study calcium distribution in astrocytes in presence of excess buffer. *International Journal of Biomathematics*, **7**(03), 1450031.
13. Jha, A. & Adlakha, N. (2015). Two-dimensional finite element model to study unsteady state Ca 2+ diffusion in neuron involving ER LEAK and SERCA. *International Journal of Biomathematics*, **8**(01), 1550002.
14. Joshi, H., & Jha, B. K. (2018, May). Fractional reaction diffusion model for Parkinson's disease. *International Conference on ISMAC in Computational Vision and Bio-Engineering*. Springer, Cham, 1739–1748. .
15. Joshi, H. & Jha, B. K. (2020). Fractional-order mathematical model for calcium distribution in nerve cells. *Computational and Applied Mathematics*, **39**(2), 1–22.
16. Kotwani, M. & Adlakha, N. (2017). Modeling of endoplasmic reticulum and plasma membrane Ca 2+ uptake and release fluxes with excess buffer approximation (EBA) in fibroblast cell. *International Journal of Computational Materials Science and Engineering*, **6**(01), 1750004.
17. Kumar, H., Naik, P. A. & Pardasani, K. R. (2018). Finite element model to study calcium distribution in T lymphocyte involving buffers and ryanodine receptors. *Proceedings of the National Academy of Sciences, India Section A: Physical Sciences*, **88**(4), 585–590.
18. Kusters, J. M. A. M., Cortes, J. M., Van Meerwijk, W. P. M., Ypey, D. L., Theuvenet, A. P. R. et. al. (2007). Hysteresis and bistability in a realistic cell model for calcium oscillations and action potential firing. *Physical review letters*, **98**(9), 098107.

19. Lembong, J., Sabass, B., Sun, B., Rogers, M. E. & Stone, H. A. (2015). Mechanics regulates ATP-stimulated collective calcium response in fibroblast cells. *Journal of the royal society interface*, **12**(108), 20150140.
20. Manhas, N. & Pardasani, K. R. (2014). Mathematical model to study IP_3 dynamics dependent calcium oscillations in pancreatic acinar cells. *Journal of Medical Imaging and Health Informatics*, **4**(6), 874–880.
21. Manhas, N., Sneyd, J. & Pardasani, K. R. (2014). Modelling the transition from simple to complex Ca^{2+} oscillations in pancreatic acinar cells. *Journal of biosciences*, **39**(3), 463–484.
22. McAnulty, R. J. (2007). Fibroblasts and myofibroblasts: their source, function and role in disease. *The international journal of biochemistry & cell biology*, **39**(4), 666–671.
23. Mukherjee, S., Kolb, M. R., Duan, F. & Janssen, L. J. (2012). Transforming growth factor–β evokes Ca^{2+} waves and enhances gene expression in human pulmonary fibroblasts. *American journal of respiratory cell and molecular biology*, **46**(6), 757–764.
24. Naik, P. A. & Pardasani, K. R. (2015). One dimensional finite element model to study calcium distribution in oocytes in presence of VGCC, RyR and buffers. *Journal of Medical Imaging and Health Informatics*, **5**(3), 471–476.
25. Naik, P. A. & Pardasani, K. R. (2016). Finite element model to study calcium distribution in oocytes involving voltage gated Ca^{2+} channel, ryanodine receptor and buffers. *Alexandria Journal of Medicine*, **52**(1), 43–49.
26. Naik, P. A. & Pardasani, K. R. (2018). 2D finite-element analysis of calcium distribution in oocytes. *Network Modeling Analysis in Health Informatics and Bioinformatics*, **7**(1), 1–11.
27. Neher, E. (1986). Concentration profiles of intracellular calcium in the presence of a diffusible chelator. *Experimentell Brain Research*, **14**, 80–96.
28. Panday, S.& Pardasani, K. R. (2013). Finite element model to study effect of advection diffusion and Na+/Ca^{2+} exchanger on Ca^{2+} distribution in oocytes. *Journal of medical imaging and health informatics*, **3**(3), 374–379.
29. Panday, S. & Pardasani, K. R. (2014). Finite element model to study the mechanics of calcium regulation in oocyte. *Journal of Mechanics in Medicine and Biology*, **14**(02), 1450022.
30. Pathak, K. B. & Adlakha, N. (2015). Finite element model to study calcium signalling in cardiac myocytes involving pump, leak and excess buffer. *Journal of Medical Imaging and Health Informatics*, **5**(4), 683–688.
31. Pathak, K. & Adlakha, N. (2016). Finite element model to study two dimensional unsteady state calcium distribution in cardiac myocytes. *Alexandria Journal of Medicine*, **52**(3), 261–268.
32. Phan, S. H. (2008). Biology of fibroblasts and myofibroblasts. *Proceedings of the American Thoracic Society*, **5**(3), 334–337.
33. Roach, K. M. & Bradding, P. (2020). Ca^{2+} signalling in fibroblasts and the therapeutic potential of KCa3. 1 channel blockers in fibrotic diseases. *British Journal of Pharmacology*, **177**(5), 1003–1024.
34. Schmeitz, C. D., Hernandez-Vargas, E. A., Fliegert, R., Guse, A. H. & Meyer-Hermann, M. (2013). A mathematical model of T lymphocyte calcium dynamics derived from single transmembrane protein properties. *Frontiers in immunology*, **4**, 277.
35. Sherman, A., Smith, G. D., Dai, L. & Miura, R. M. (2001). Asymptotic analysis of buffered calcium diffusion near a point source. *SIAM Journal on Applied Mathematics*, **61**(5), 1816–1838.
36. Singh, N. & Adlakha, N. (2018). Effect of Source Geometry on Interdependent Calcium and Inositol 1; 4; 5-Trisphosphate Dynamics in a Cardiac Myocyte Cell. *International Conference on Mathematical Modelling and Scientific Computation*, Springer, Singapore, 75–83.

37. Singh, N. & Adlakha, N. (2019). A mathematical model for interdependent calcium and inositol 1, 4, 5-trisphosphate in cardiac myocyte. *Network Modeling Analysis in Health Informatics and Bioinformatics*, **8**(1), 1–15.
38. Smith, G. D. (1996). Analytical steady-state solution to the rapid buffering approximation near an open Ca^{2+} channel. *Biophysical journal*, **71**(6), 3064–3072.
39. Stamatakis, M. & Mantzaris, N. V. (2006). Modeling of ATP-mediated signal transduction and wave propagation in astrocytic cellular networks. *Journal of theoretical biology*, **241**(3), 649–668.
40. Sun, G. X., Wang, L. J., Xiang, C. & Qin, K. R. (2013). A dynamic model for intracellular calcium response in fibroblasts induced by electrical stimulation. *Mathematical Biosciences*, **244**(1), 47–57.
41. S. Tewari & K.R. Pardasani (2009). Finite difference model to study the effects of Na^{+} influx on cytosolic Ca^{2+} diffusion. *International journal of Biological and Medical Sciences*, 205–209.
42. Tewari, S. & Pardasani, K. R. (2010). Finite element model to study two dimensional unsteady state cytosolic calcium diffusion in presence of excess buffers. *IAENG International Journal of Applied Mathematics*, **40**(3), 108–112.
43. TEWARI, S. G. & Pardasani, K. R. (2012). Modeling effect of sodium pump on calcium oscillations in neuron cells. *Journal of Multiscale Modelling*, **4**(03), 1250010.
44. Torres, J. J., Cornelisse, L. N., Harks, E. G. A., Van Meerwijk, W. P. M., Theuvenet, A. P. R. et. al. (2004). Modeling action potential generation and propagation in NRK fibroblasts. *American Journal of Physiology-Cell Physiology*, **287**(4), C851–C865.
45. Tripathi, A. & Adlakha, N. (2011). Finite volume model to study calcium diffusion in neuron cell under excess buffer approximation. *International J. of Math. Sci. and Engg. Appls. (IJMSEA)*, **5**, 437–447.
46. Vaeth, M., Kahlfuss, S. & Feske, S. (2020). CRAC channels and calcium signaling in T cell-mediated immunity. *Trends in immunology*, **41**(10), 878–901.
47. Van Zoelen, E. J., van Rotterdam, W., van de Wetering, R. A. & Heldin, C. H. (1993). Differential Effects of PDGF Isoforrns on Proliferation of Normal Rat Kidney Cells. *Growth Factors*, **9**(4), 329–339.
48. Wagner, J. & Keizer, J. (1994). Effects of rapid buffers on Ca^{2+} diffusion and Ca^{2+} oscillations. *Biophysical journal*, **67**(1), 447–456.
49. Wagner, J., Fall, C. P., Hong, F., Sims, C. E., Allbritton, N. L., Fontanilla, R. A. et. al. (2004). A wave of IP_3 production accompanies the fertilization Ca^{2+} wave in the egg of the frog, Xenopus laevis: theoretical and experimental support. *Cell calcium*, **35**(5), 433–447.
50. Öziş, T., Aksan, E. N. & Özdeş A. (2003). A finite element approach for solution of Burgers' equation. *Applied Mathematics and Computation*, **139**(2-3), 417–428.

